Pergamon

Journal of Structural Geology, Vol. 17, No. 12, pp. 1757 to 1769, 1995

0191-8141/95 $9.50+0.00

0191-8141(95)00067-4

Porosity network of a ductile shear zone

YVES GÉRAUD, JEAN-MICHEL CARON and PIERRE FAURE

Laboratoire de Sciences de la Terre, URA CNRS 726, ENS Lyon et UCB Lyon 1, 46, allée d'Italie, F-69364 Lyon Cedex 07, France

(*Received* 15 *June* 1994; *accepted in revised form* 1 *June* 1995)

Abstract—The permeability of ductile shear zones is assumed to be significantly higher than that of surrounding undeformed rocks, although lower than that of fracture systems. This assumption, which results indirectly from geochemical mass balance calculations, is checked in this paper by the tomography of the porosity network in a metre-wide deformation zone. Combined techniques, with different resolutions ranging between 1 mm and 1 μm, are used on oriented thin sections and drilled cores: nuclear magnetic resonance (NMR) imaging, X-ray tomodensitometry (medical scanner), mercury injection porosimetry and scanning electron microscopy (SEM).

We show that porosity ranges between 1% at the margins and 8% in the median part, with throat diameters between 0.8 and 0.01 μm. The porosity network is heterogeneous, mixed (cracks and tubes) and anisotropic. Cracks are common in the less deformed samples, whereas tubes prevail in the more strained median part. The porosity network is anisotropic, especially in the high strained samples, where tubes are preferentially oriented in the c-planes. This shape duality is expected to influence the transfer properties of the studied rocks. Estimates of related permeability are about 5×10^{-16} and 5×10^{-15} m^2 in the shear zone, and about 10^{-17} m^2 in the less deformed granite. We discussed the occurrence of such a contrast at depth between the shear zone and the granite.

INTRODUCTION

Migration of water-rich fluids is known to take place in the upper part of the Earth's crust through fracture systems (Fyfe *et al.* 1978, Brace & Kohlstedt 1980, Rice 1992). The permeability, about 10^{-12}–10^{-14} m^2, depends on the size and interconnection of the fractures (Long & Witherspoon 1985, Gavrilenko & Gueguen 1989). Fluid flow is also assumed from indirect geochemical arguments to be channelled in continuous but heterogeneous rocks such as ductile shear zones (Etheridge *et al.* 1983, Marquer & Burkhard 1992). Indeed, shear zones are frequently correlated with mineralogical and chemical differentiation with respect to their surrounding rocks considered as protoliths (e.g. Kerrich *et al.* 1980, Potdevin & Marquer 1987). Mass balance calculations from elements (principally Si, K, Na, Ca, Mg) as well as stable isotopes imply pervasive fluid flow over distances of up to several km (Dipple *et al.* 1990). Estimates of fluid/rock ratios and of flow durations predict average permeabilities of 10^{-15}–10^{-17} m^2 (Dipple & Ferry 1992).

The purpose of this paper is to document the geometric features of the porosity network in a ductile shear zone by direct observations at different scales. Several techniques are used to measure the shape, the size and the distribution of the pores. These measurements make it possible to estimate the permeability in this heterogeneous continuous medium.

STRUCTURES

Geological setting

The studied shear zone is located in the northwestern French Massif Central, 3 km south of Dun-le-Palestel (Fig. 1). It belongs to a leucogranitic belt, 1–4 km wide, which extends east–west over 35 km along the Marche transcurrent zone. This syn-kinematic granitic body was emplaced about 320–310 Ma ago during a Late Variscan stage and is pervasively and heterogeneously deformed (Quenardel *et al.* 1988). Cataclasites are restricted to the immediate vicinity of the Marche fault. Ductile mylonites and blastomylonites constitute metre-wide vertical zones parallel to the fault. We have taken a series of samples in a profile continuously across one of these wrench mylonitic shear zones.

Deformation

Two sub-vertical planar anisotropies are well developed in the studied shear zone (Figs. 2a & b), as described frequently in mylonitized granites (e.g. Berthé *et al.* 1979). One anisotropy, referred to as 'C-surfaces', is parallel to the margins and strikes east–west (N95–100°) throughout the deformation zone. It corresponds to spaced slip planes on which the displacement is marked by sub-horizontal striations (plunge 15–20°E). The other anisotropy, described as '*S*-surfaces', is a schistosity that curves from N130° outside the zone to N105° in its median part. It traces the *XY* planes of flattening perpendicular to the short axis of the finite strain ellipsoid, between the *C*-surfaces (Ramsay & Graham 1970).

The bulk geometry of this heterogeneous ductile zone is compatible with simple shear deformation. The asymmetry between *S*- and *C*-surfaces indicates a sinistral displacement. Assuming from the relationship between minerals and microstructures that both surfaces developed simultaneously, we use the angle θ between *S*- and *C*-surfaces as an approximate estimation of the shear

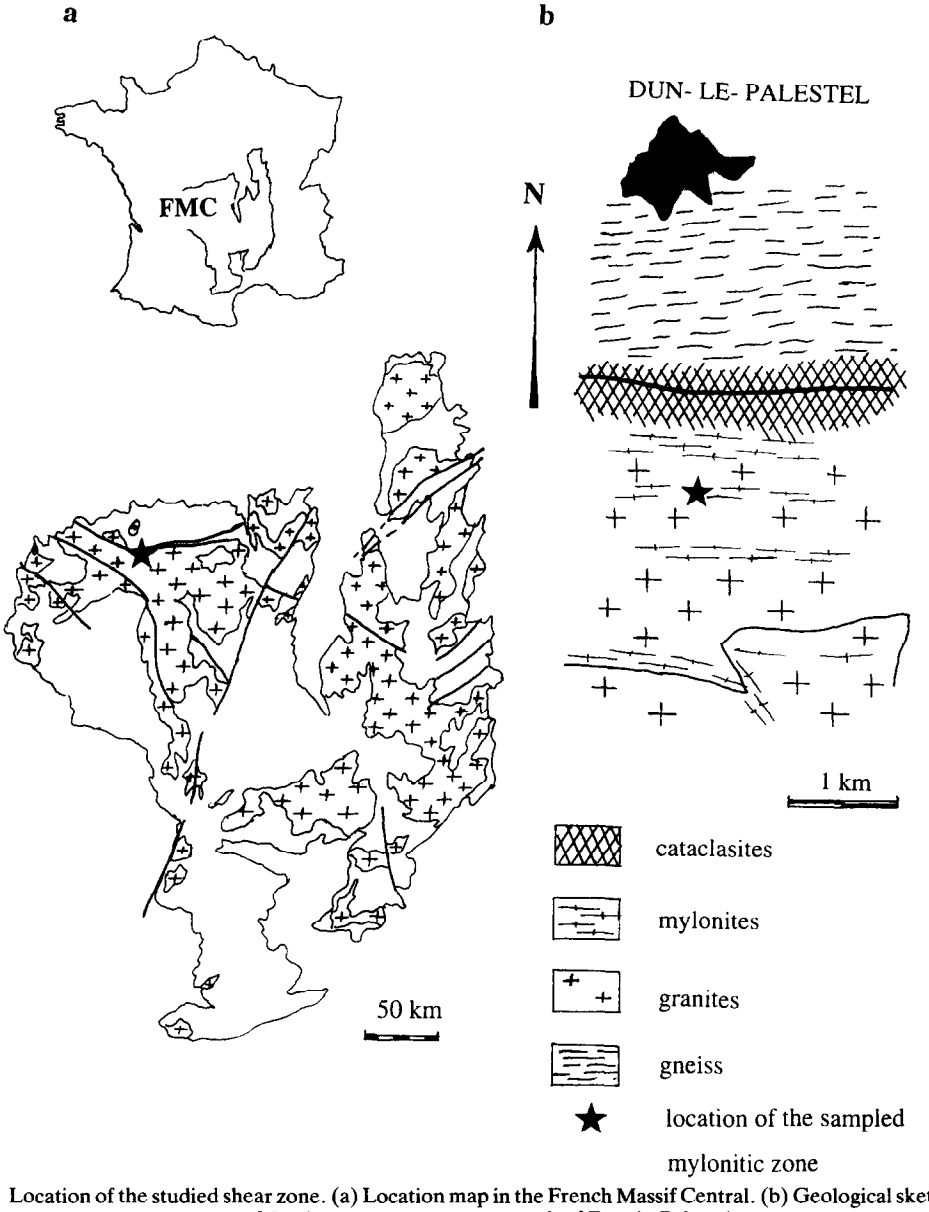

Fig. 1. Location of the studied shear zone. (a) Location map in the French Massif Central. (b) Geological sketch map of the Marche transcurrent zone, south of Dun-le-Palestel.

strain (with $\gamma = 2/\tan 2\theta$; Ramsay & Graham 1970). This shear strain ranges from 0.5 at the margins to 10 in the core, with a higher gradient on the northern side than on the southern one (Fig. 5a). Together with this shear strain variation, the spacing of the *C*-surfaces decreases from about 1 cm at the margins to less than 1 mm in the median (Fig. 5b). The less strained margins, which represent our reference protolith, are thus not deformation-free. Their fabric is considered to result from a magmatic deformation stage (Rey *et al.* 1994).

The following structures fix a reference frame of planes and axis for orientation and position (Fig. 6): the *C*-surfaces define the displacement plane ('*c*-planes'), the *b*-plane is perpendicular to the *c*-plane and parallel to the displacement direction (striations) and the *a*-plane is perpendicular to the displacement direction. The axes *a*, *b* and *c* are perpendicular to respectively the *a*-, *b*- and *c*-planes. The origin of the *c*-axis is taken where the shear strain is the highest. Locations are referred to either the distance to the origin or the shear strain value.

Minerals and microstructures

The evolution of the microstructures and their relationships with the minerals are briefly described from optical studies of thin sections parallel to *a*-, *b*- and *c*-planes (Figs. 3a & b).

The least deformed granite (sample No. 8) is composed of quartz aggregates (30%), K-feldspar grains (24–26%) about 1 cm long, oligoclase (25–29%), biotite (4–5%) and muscovite (12–15%), with minor apatite and zircon. With increasing strain, the amount of quartz and biotite does not change significantly. By contrast, the K-feldspar and plagioclase content decreases down to 14–17%, while white mica constitutes more than 35% of the mylonite (Fig. 7a). This type of evolution, characterized by transformation of feldspars into phyllosili-

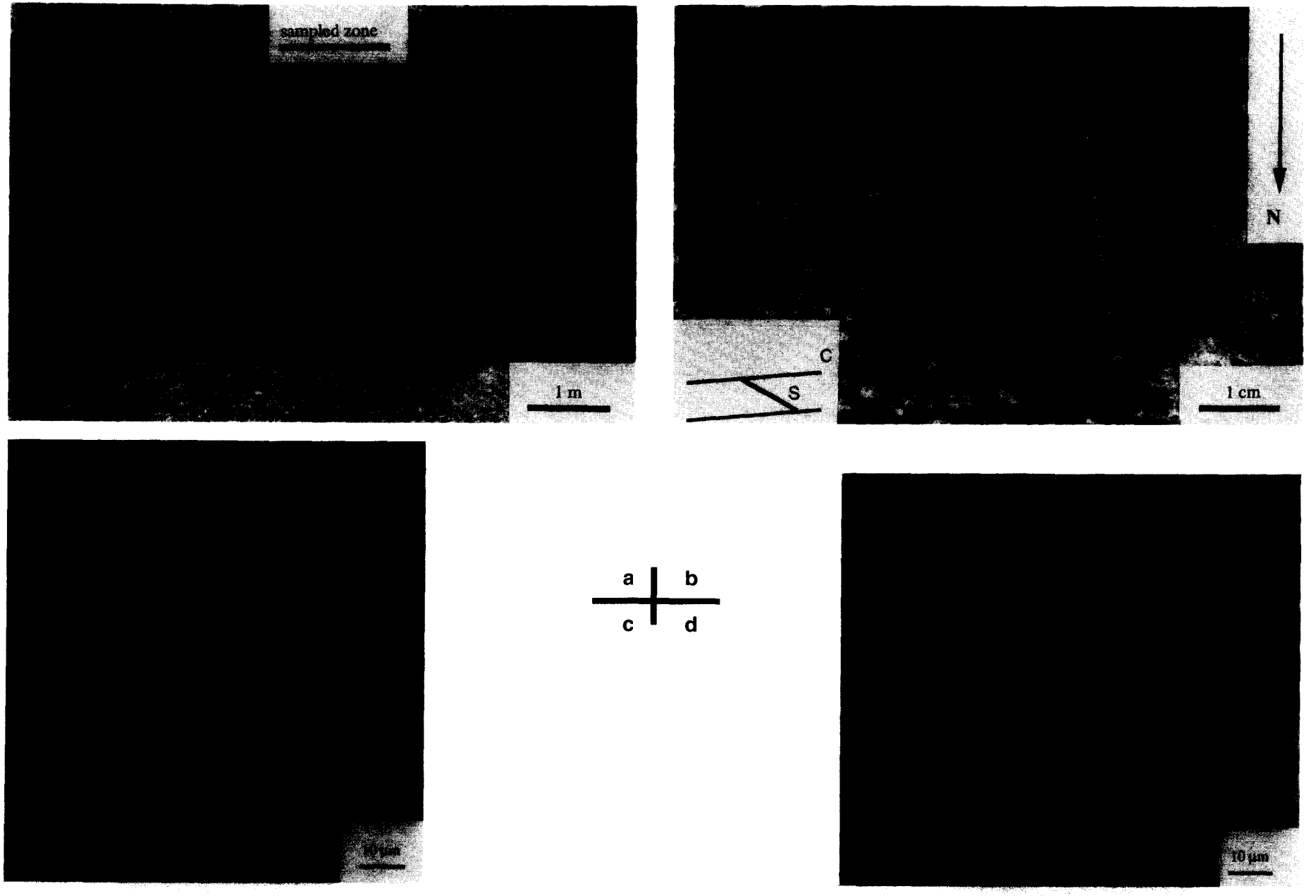

Fig. 2. (a) General view toward the east of the studied shear zone. (b) C–S fabric in the shear zone (east; to the left of the photograph). (c) Crack network in sample No. 1 (high magnification SEM image). (d) Intercrystalline tube network in sample No. 5 (high magnification SEM image); the tubes trend perpendicularly to the figure and exhibit circular cross-sections.

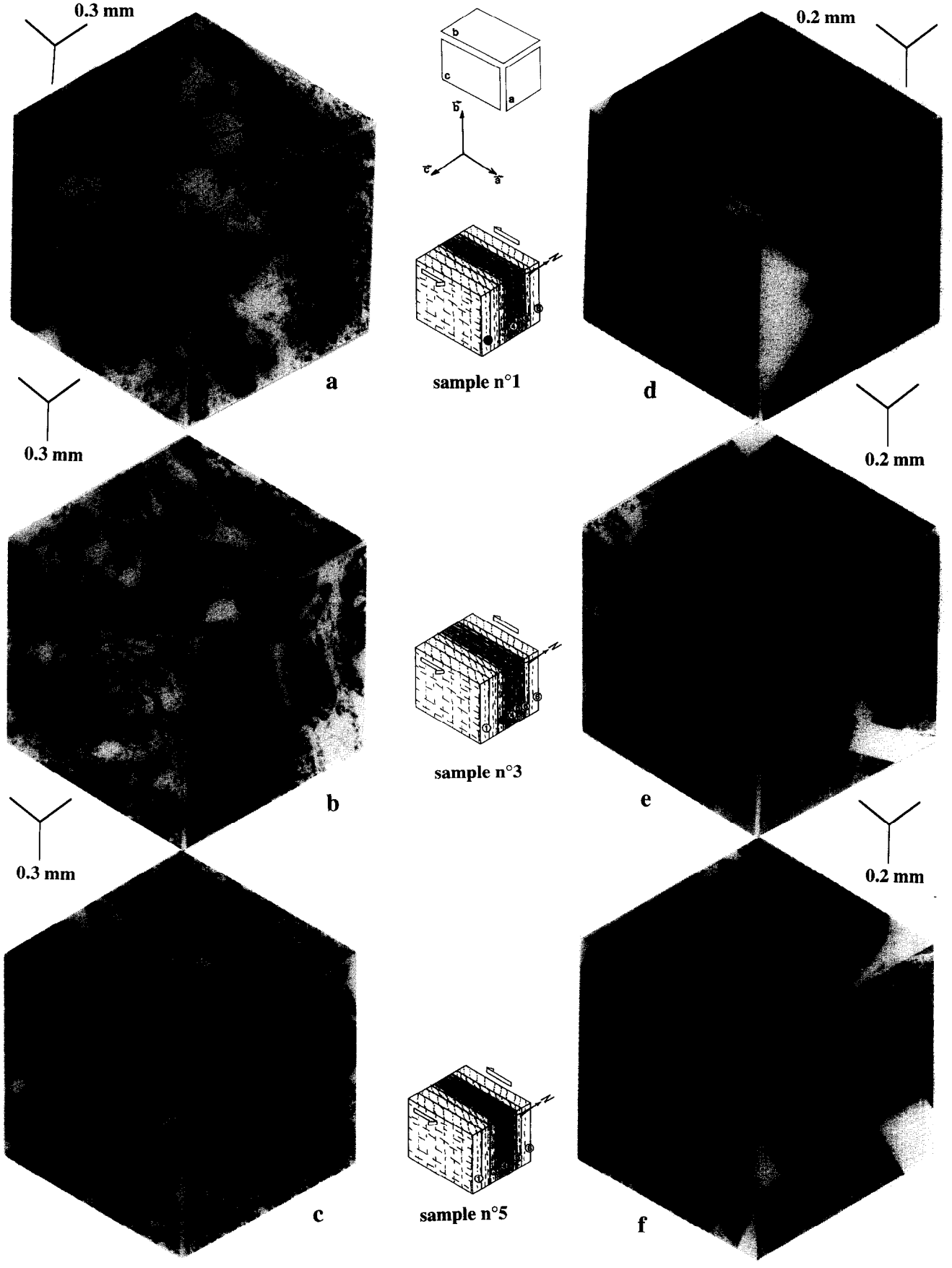

Fig. 3. (a)–(c) Photomosaics of the microstructures in sample Nos 1, 3 and 5 in the three reference planes, illustrating the evolution of the fabric with increasing strain. (d)–(f) Scanning electron microscopy photomosaics of the same samples, imaging the porosity network (in white) at higher magnification. The location of the samples is indicated in the drawing of the shear zone with black dots.

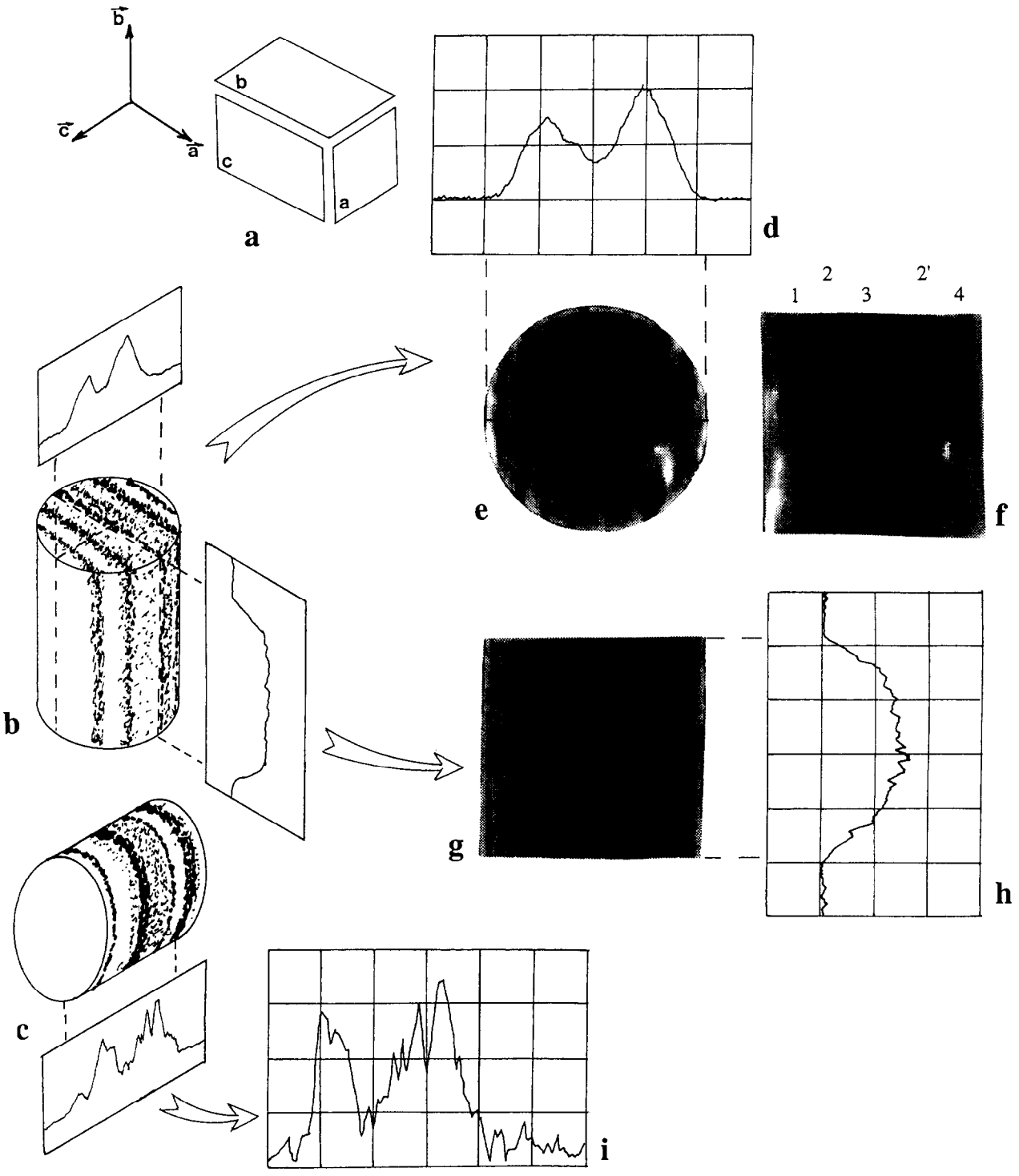

Fig. 4. The NMR profiles and scanner images of the high strain sample No. 5. (a) Reference frame. (b) Sketch of a core parallel to the *b*-axis (representing the mineralogical layering) and of two NMR cumulative profiles oriented as the reference planes *a* and *c*. (c) Sketch of a core parallel to the *c*-axis, and of a NMR cumulative profile in the *a*-plane. (d) The NMR profile along the *c*-axis (abscissa) of the *b*-core (transverse profile); the peaks correspond to high water content in feldspar–mica ribbons, grey patches are K-feldspars, and white spots are micas. (f) Scanner image of an *a*-surface of the same *b*-core [grey levels as in (e)]. (g) Scanner image of a C-surface of the same *b*-core; this section on a K-feldspar layer is parallel to the mineralogic layering, which is therefore not visible. (h) The NMR profile along the *b*-axis (ordinate) of the *b*-core (longitudinal profile); (i) NMR profile along the *c*-axis (abscissa) of the *c*-core.

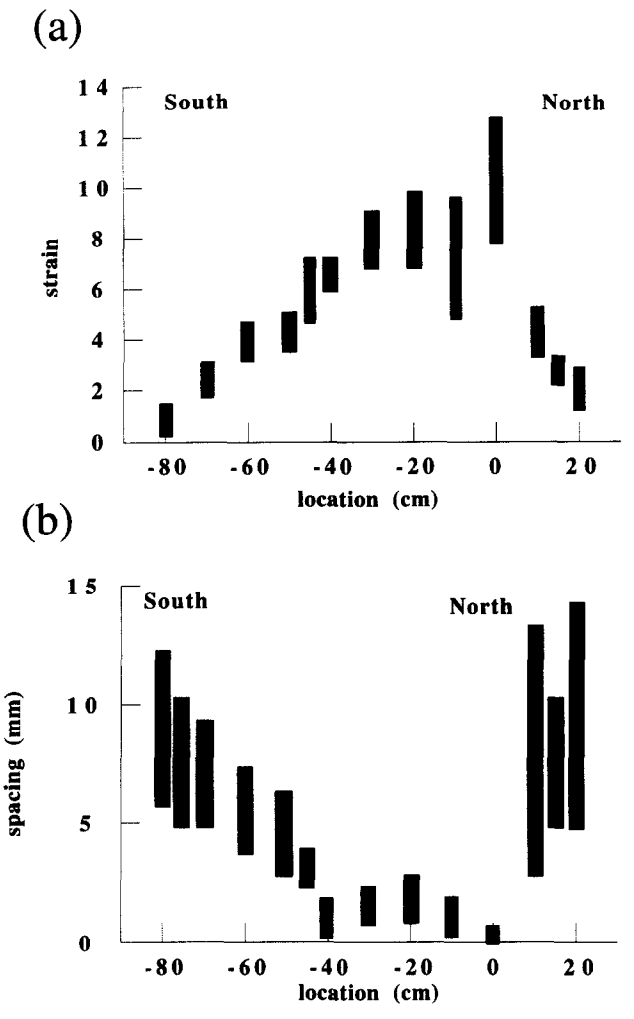

Fig. 5. (a) Shear strain values measured over the shear zone. The origin (0 cm) is chosen at maximum shear strain. (b) Spacing of the C-surfaces through the shear zone.

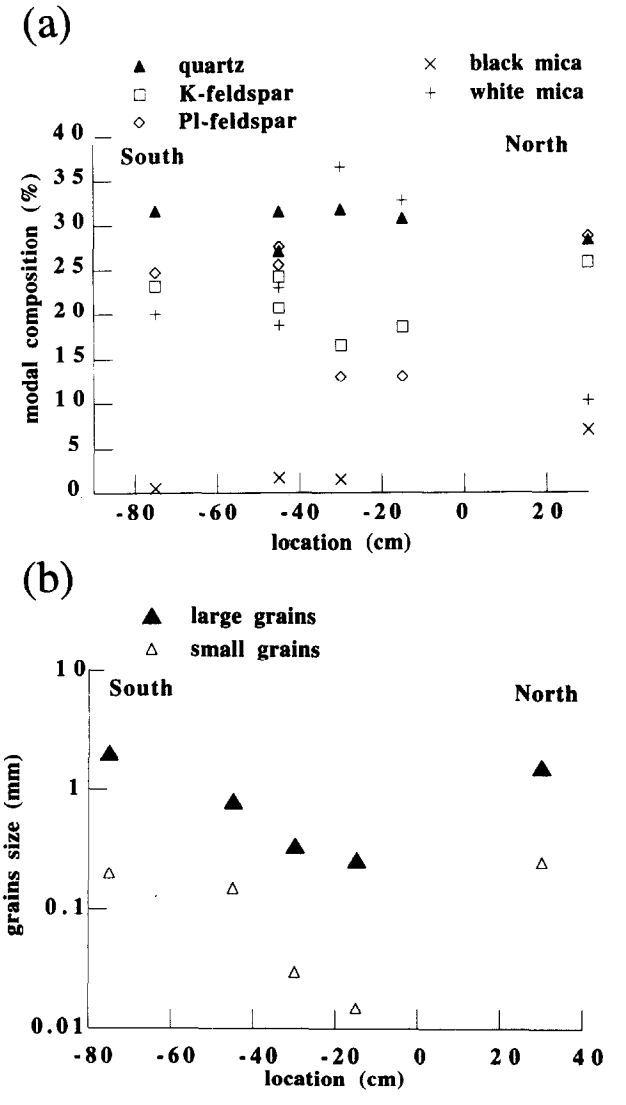

Fig. 7. (a) Variation of the modal composition over the shear zone. (b) Variation of the grain size over the shear zone.

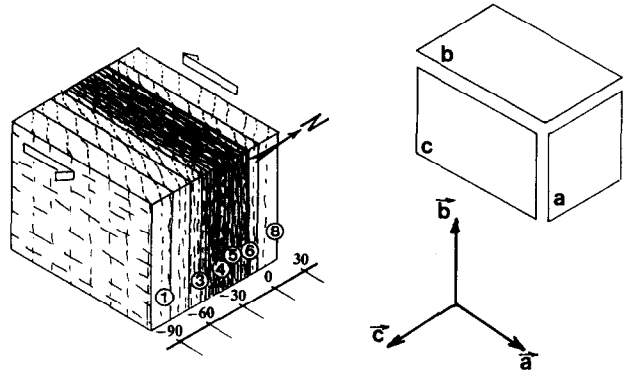

Fig. 6. Reference frame used for sampling, composed of three planes and three axes. Numbers refer to studied samples.

cates, has been described for mylonitization of granitoids (e.g. Kerrich *et al.* 1980, Marquer *et al.* 1985).

Grain size reduction is clearly related to increasing deformation in the shear zone and affects the large as well as the small grains (Fig. 7b). In the less deformed samples (Nos 8 & 1) large grains of quartz, feldspar and mica are 1–10 mm wide. The size of smaller grains of quartz, plagioclase and muscovite ranges between 0.1 and 0.3 mm. The grain size distribution in the mylonite (sample Nos 5 & 6) is also bimodal, with 100 μm-large K-feldspars and 10 μm-large quartz, feldspars and micas. Moreover, in the mylonite, quartz on the one hand and feldspar–micas on the other, constitute alternating ribbons that are 1–5 mm wide and generally bounded by discontinuous seams of micas. This grain size reduction was accommodated by deformation–recrystallization processes that led to different microstructures (Lespinasse 1984, FitzGerald & Stunitz 1993).

In the moderate deformation stages, K-feldspars are broken by tension gashes filled with quartz, the orientation of which is compatible with the sense of shear (mode I failure). Bending and undulating extinction of feldspars is common. With increasing strain, sub-grains develop and are progressively disoriented. This process of grain size reduction occurs preferentially at the rim of the K-feldspar phenoclasts. It leads to core and mantle microstructures with asymmetric trails that are consistent with the sense of shear. The plagioclase grains display the same variety of microstructures as the K-feldspars. They are also deformed by mechanical twinning and kinking.

In the less deformed samples some substructures, such as sub-prismatic deformation bands and scarce sub-basal deformation lamellae, are visible in quartz grains. With increasing deformation, sub-grains develop and are progressively disoriented. Grain boundaries are lobate. At a γ value of about two, elongate aggregates are composed of quartz grains with a well-developed lattice fabric. The shape-preferred orientation of the grains parallels the *S*-surfaces, where they are the material support of the mineral lineation. At high shear strain, the shape of the grains in the aggregates is isodiametric.

Micas are rotated, bent and locally kinked. New, small grains grow along the grain and sub-grain boundaries of muscovite and biotite. Parallel to the *S*- and *C*-surfaces, they delimit lenses and ribbons of quartz and feldspars.

The fabric of the studied samples is thus strongly anisotropic at all scales throughout the shear zone. It results from ductile deformation that occurred under the stability conditions of biotite, at about 400–450°C and 2–3 kbar (M. Cathelineau, oral communication). These samples are not affected locally by later brittle deformation.

POROSITY

The porosity of the rocks in this shear zone is studied by a combination of techniques, carried out on oriented sections and on core samples drilled along the three reference axes (Fig. 6). Nuclear magnetic resonance (NMR) and X-ray tomodensitometry (medical scanner) image the distribution of water in the cores with a resolution of about 1 mm. Mercury injection measurements give access to the size distribution of the connected voids between 0.01 and 1000 μm. Scanning electron microscopy (SEM) shows the shape, the orientation and the repartition of the voids on sections, with a resolution down to 1 μm.

Nuclear magnetic resonance imaging

Over the past decade, NMR imaging has spread as a medical and biological tool that provides detailed spatial images of organs. Most applications of NMR imaging to material sciences were dedicated to construction materials (Gummerson *et al.* 1979) and imaging of water in porous rocks and concretes (e.g. Guillot *et al.* 1991, Jeandey *et al.* 1991). An introduction to the principles of NMR imaging and its limitations is given by Guillot & Dupas (1992). Our results were acquired with an NMR imaging machine (with a field of 0.13 T) at the NMR Laboratory of the Université Claude Bernard in Lyon. The images were obtained using the spin-echo method with a magnetic field gradient of 3×10^{-7} T m^{-1}. The signal depends primarily on the water content of the sample, i.e. the porosity, and to a smaller extent on the mineralogical composition.

Measurements were made on 35 mm diameter cores. The samples were first desiccated at 50°C for 24 h and deaerated with a vacuum pump. They were then saturated with water. Because of the low water content of these rocks, it was impossible to obtain direct three-dimensional images of water repartition. The NMR signal intensity of the whole sample was projected onto an observation axis resulting in two types of profiles of the bulk water content: one along the core longitudinal section and one of the transverse section.

The distribution of water at the level saturation was strongly heterogeneous in the most strained mylonitic samples. There are clear differences between the qualitative water content profiles in directions 'b' and 'c' of sample No. 5 (Fig. 4b). Along the 'b' direction, the profile is a plateau, which corresponds to a regular water content (Fig. 4h). By contrast, peaks are observed along the 'c' direction on both *b*-core (transverse profile, Fig. 4d) and *c*-core (longitudinal profile, Fig. 4i). This heterogeneous distribution of water in 0.5 cm-wide levels is quite consistent with the macroscopic mineralogical layering of the mylonite, where the quartz ribbons correspond to the low porosity layers (low water content) and the feldspar–mica ribbons correspond to the high porosity layers (high water content). In the less strained samples (such as No. 8), the NMR cumulative profiles are irregular in all directions, because of the three-dimensional, lense-shaped structure.

X-ray tomodensitometry

This non-destructive technique was introduced for medical purpose before being adapted to rock analysis (Raynaud *et al.* 1989, Géraud *et al.* 1992, Johns *et al.* 1993). It is based on measuring the attenuation of X-ray beams, which defines a radiologic density. The results were obtained with the CGR ND 8000 scanner at the Laboratoire de Mécanique et d'Acoustique, Marseille, France, using a 70 keV beam. The images correspond to 2 mm-thick sections perpendicular to the core axis. Longitudinal sections were computed from the data of the transverse sections.

With a resolution of about 1 mm^3, the radiologic densities depend on the mineralogical composition rather than on the porosity. The low radiologic densities, which give dark spots on the two-dimensional images (Figs. 4e–g), correspond to quartz and plagioclase. The grey patches are K-feldspars and the white spots are micas. For the mylonitic sample No. 5, the scanner images confirm the mineralogical layered structure where K-feldspar ribbons are continuous in the *c*-planes (Fig. 4g), and quartz and micas are discontinuously distributed with micas concentrated at the quartz–feldspar interfaces (Figs. 4e & f). Comparison of scanner results with the NMR images of the same core samples shows that high water content and high porosity levels (NMR) are related to the feldspar and mica rich layers (scanner). By contrast, the low porosity levels are associated with quartz.

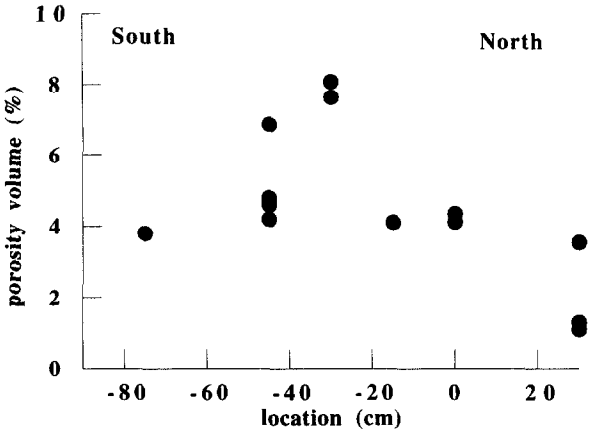

Fig. 8. Connected porosity values over the shear zone, derived from mercury injection measurements.

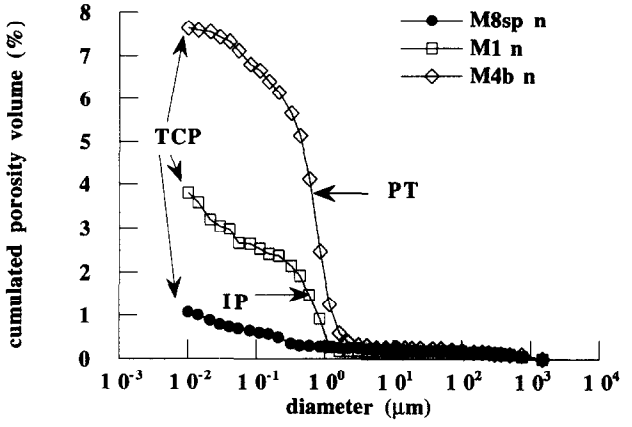

Fig. 9. Cumulative porosity curves. A cored cylinder of rock (d = 25 mm, L = 20 mm) is placed in sample chamber and de-aerated to a pressure of 15 μm of mercury. Mercury is raised in a capillary from the top of the sample chamber. Air is admitted in increments to increase the pressure on the mercury surrounding the sample up to 1 bar (this is the low pressure run). Then the mercury pressure is increased up to 300 MPa in a high pressure cell. The volume of invading mercury for each pressure increment is measured and plotted on the injection curve. The injected mercury invades progressively (step by step) pores with decreasing diameter (values from the right to the left on the figure). See text for a detailed comment of the results; TCP = the total connected porosity obtained at the highest mercury pressure (3200 Mpa); PT = percolation threshold, defined as the inflection point of the cumulative injection curve (Katz & Thompson 1987); IP = the first inflection point of the bimodal curve of the intermediate strained sample (No. 1), this value is used as percolation threshold for the permeability calculation (Table 1).

Mercury injection porosimetry

This method (Van Brakel *et al.* 1981, Guyon *et al.* 1984, Matthews *et al.* 1993) allows porosity and pore size to be estimated by measuring the volume of mercury injected in previously desiccated and de-aerated samples. The measurements of the injection pressure and of the injected mercury volume were made by steps of increasing pressure. The throat size is related to mercury pressure by the Washburn equation $d = (-4\sigma \cos \theta)/P$, where d is the throat diameter (i.e. the diameter of the pores or of the tubes or the width of the cracks), σ the air–mercury inter-facial tension (0.48 N m^{-1}), θ the contact angle between mercury and the solid phase (140°) and P the capillary mercury pressure (the measured injection pressure). A cumulative curve of the injected mercury volume was obtained as a function of the injection pressure with this technique, the cumulative porosity (i.e. the injected mercury volume) is derived as a function of the throat diameter (i.e. a function of the injection pressure). It gives the total connected porosity at the maximum pressure (150 MPa) and the distribution of throat diameters d. When this distribution is unimodal, the inflection point of the cumulative curve is assumed to correspond to the percolation threshold (Katz & Thompson 1987), i.e. the pressure and the diameter for which a continuous network of voids connects the opposite ends of the sample. This threshold value constrains the permeability (see Discussion). In the case of more complicated curves, the values of the throat diameter at the inflection points are given for comparison.

The connected porosity ranges from 1% for the lowest strain sample (No. 8) to 8% for the sample located at −30 cm (sample No. 4, Fig. 8). Shapes of the cumulative curves are different and vary with the location of the sample in the shear zone. For the lowest strain (sample No. 8, Fig. 9), the curve is unimodal, which is typical of a single type of void, with a low connected porosity (about 1.2%) and a small percolation threshold (about 0.1 μm). In the high strained samples (No. 4, Fig. 9), the curve is also unimodal, but with higher connected porosity (8%) and larger percolation threshold (about 0.3 μm). For intermediate strain values, as in sample No. 1 (Fig. 9), the curve is composite, which corresponds to the presence of two types of pores: one with a well-defined inflection point of 0.4 μm, and another which corresponds to the steep part of the curve below 0.05 μm.

Scanning electron microscopy

As for microstructures in thin section (Figs. 3a–c), the size, shape and distribution of pores were observed by SEM on three orthogonal surfaces (a-, b- and c-planes). The samples originate from different locations in the shear zone (Figs. 3d–f). These two-dimensional images permit three-dimensional shapes to be estimated. In the less deformed samples (No. 1), porosity results from cracks roughly parallel to the macroscopic C-surfaces and connected to other cracks, which are oriented as tension gashes compatible with the sinistral shear. This pattern is clear on the b-plane (Fig. 2c). Tubes are present only within feldspars where they are connected to intracrystalline cracks. In the mylonitic samples (No. 5), pores are abundant and nearly circular on the a- and b-sections. They are less common and elongated in the c-plane. In three dimensions, the shape of these pores is therefore tubular (Fig. 2d). The tubes are preferentially oriented in the C-surfaces. They appear to be principally controlled by the joints between quartz or feldspar grains and aggregates and especially at the contact with micas. For intermediate shear strain values (sample No. 3), the porosity network consists of cracks and tubes. Tubes are widespread along mica stripes and within feldspar grains. Intergranular cracks parallel mica

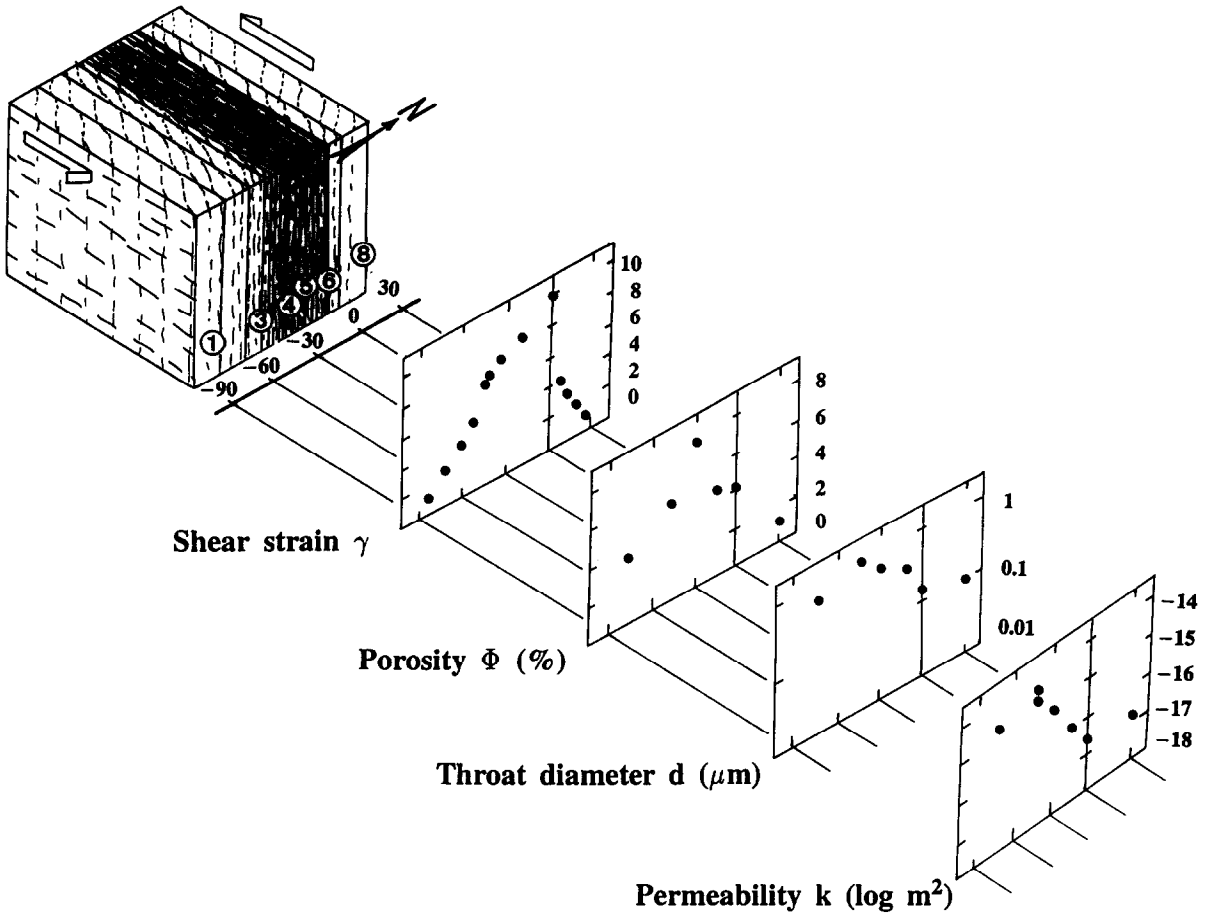

Fig. 10. Summary of the geometrical features over the shear zone. Shear strain is measured (Fig. 5a), porosity and percolation threshold are derived from mercury injection measurements and permeability is inferred from porosity data (Table 1).

boundaries and intragranular cracks are observed in feldspar clasts.

DISCUSSION

From the observations presented above, it is evident that the rocks of this mylonite zone are porous and that porosity varies with the shear strain (Fig. 10). Porosity is heterogeneous at two different scales: on the one hand, it is larger at the metre scale in the highly strained axial part of the shear zone (up to 8%) than at the less deformed margins (1–2%) and increases with grain size reduction; there is a shift between the highest porosity value and the highest strain value. On the other hand, porosity is heterogeneous at the centimetre scale in the mylonite, where it is higher in the feldspar–mica ribbons than in the quartz ribbons.

Porosity is variable, because it is composed of pores with two different shapes: cracks and tubes. Cracks occur principally in the mildly deformed margins, whereas tubes are developed in the more strongly deformed central mylonite.

The porosity network is anisotropic: cracks, and especially tubes, are preferentially oriented parallel to the C-surfaces. This preferred orientation is best developed in the central mylonite, where it tends to parallel the major finite strain axis.

Direct tomographic methods (NMR imaging and X-ray tomodensitometry) and two-dimensional observations in orthogonal planes (SEM) allow a qualitative sketch of the porosity network to be constructed that summarizes the principal features at three different locations in the studied ductile shear zone (Fig. 11).

A rigorous modelling of permeability from the porosity network would require more quantitative data that are currently not available. Nevertheless, a rough estimate of the permeabilities k can be attempted based on the connected porosities Φ and the throat diameters d. By using the following relations (Gueguen & Palciauskas 1992), we get the values listed in Table 1:

$$k = \frac{w^2\Phi}{3} \quad \text{for cracks of mean half-width } w; \quad (1)$$

$$k = \frac{r^2\Phi}{8} \quad \text{for tubes of mean radius } r. \quad (2)$$

The dimensions used for w and r are the throat diameters at the inflection points of the porosity curves. They lead to two slightly different values of k for each sample. Because of the pore shape, estimates based on w are probably more relevant to the crack porosity of sample Nos 1 and 8 while those based on r are more relevant to the tube porosity of sample Nos 4–6.

The estimated permeabilities vary between 10^{-16} and

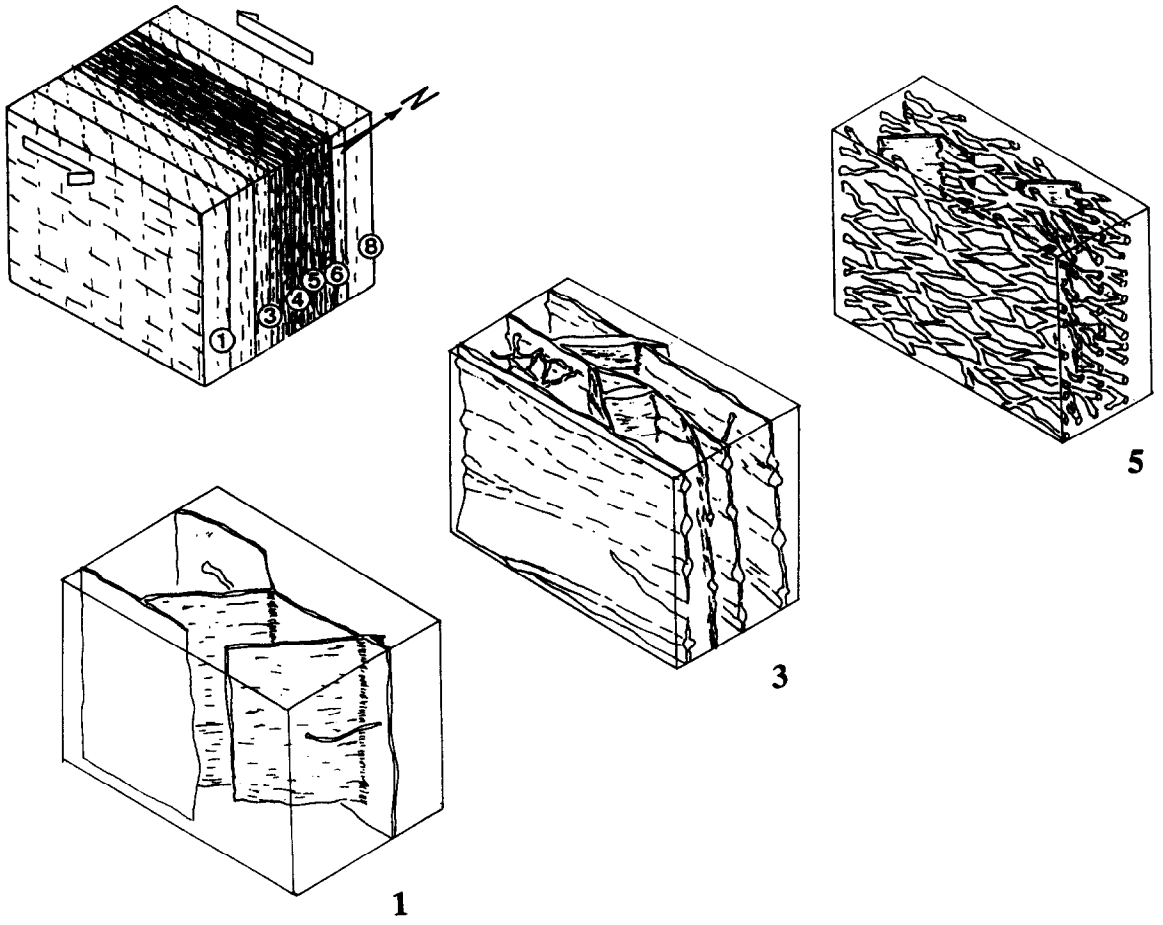

Fig. 11. Sketch of the porosity network in three samples from the shear zone. It consists mainly of cracks in the gently deformed margins (sample No. 1), tubes in the strongly deformed central mylonites (sample No. 5) and a mixed network (cracks and tubes) in the intermediate sample (No. 3).

Table 1. Porosities, throat diameters and estimated permeabilities in the studied samples

Sample	Distance (x) cm	Shear strain (γ)	Porosity (Φ) %	Half-width (w) or radius (r) μm	Permeability (k) $\frac{\bar{w}^2\Phi}{3}$ 10^{-15} m^2	$\frac{\bar{r}^2\Phi}{8}$ 10^{-15} m^2
1	−75	1.5	3.8	0.4	2	0.7
3a			6.8	0.5	5.7	2.1
$3b_1$	−45	6	4.75	0.4	2.5	1
$3b_2$			4.25	0.5	3.5	1.3
3c			4.6	0.55	4.6	1.7
4a	−30	7.5	8	0.3	1.2	**0.45**
4b			7.6	0.3	2.3	**0.8**
5	−15	8	4.1	0.125	0.2	**0.08**
6a	0	10	4.45	0.04	0.025	**0.009**
6b			4.12	0.075	0.077	**0.029**
8a			1.3	0.1	**0.043**	0.016
8b	30	<1	1.1	0.05	**0.009**	0.003
8c			1.15	0.05	**0.01**	0.004

5×10^{-15} m^2 in the southern part of the shear zone (sample Nos 1–5). These permeabilities are one or two orders of magnitudes higher than in the surrounding little deformed granite (about 10^{-17} m^2, sample No. 8), in which it is slightly higher than the permeability of average quarried granite (between 10^{-18} and 10^{-19} m^2; Brace 1980, Géraud *et al.* 1993, Morrow & Lockner 1994). In addition, the calculated permeability is significantly lower (1–3 $\times$ 10^{-17} m^2) in the highest strained sample No. 6 than in the rest of the shear zone. This last low permeability results from narrow throat diameters and seems to be related to a locally high silica content. This feature may be related to a locally greater amount of quartz-rich ribbons, or to silica deposition in the voids. Furthermore, the evolution stage of this shear zone to which the measured porosity is relevant is questionable. Ductile deformation occurred at depth, whereas the samples characterize the current state of the fresh exposure. Mass transfer and fluid flow may thus have taken place at different stages during the evolution

of this shear zone: (1) during the deformation which gave rise to it; (2) during hydrothermal events related to subsequent uplift; and (3) during surface weathering.

In its current state, the structure of the porosity network is clearly variable over the shear zone and the inferred permeabilities are expected to be higher in the strained samples (Nos 1–5) than in the surrounding, little-deformed granite. Present fluid transfer would thus be channelled along the metre-wide structural heterogeneity constituted by the shear zone. Furthermore, chemical and mineralogical observations show that the void structure probably has not been modified by significant mass transfer subsequently to the ductile deformation stage. Measurements on Sr and Rb isotopes performed on 12 samples from this shear zone define a quite good isochron (B. Luais *et al.* in preparation), the age of which is sub-contemporaneous with granite emplacement (Quenardel *et al.* 1988). The chemical system constituted by this shear zone was thus not opened after deformation. In addition, a systematic search by X-ray diffraction did not reveal the presence of minerals provided for by weathering in these samples and thus sub-surface geometrical modification of the porosity network by recent mineral deposition is unlikely. The main difference between the initial deformation-related state and the current state of the porosity network results from the mechanical effect of uplift. Unloading permeability is experimentally known to decrease with increasing confining pressure, which causes the closure of voids. This pressure sensitivity depends on the shape of the voids and, for cracks in granite, the difference in permeability is of two or three orders of magnitude between the surface and 300–400 MPa of effective confining pressure (Brace *et al.* 1968, Bernabé 1986, Morrow & Byerlee 1992, Morrow & Lockner 1994). Following the model of Walsh (1965), pores and tubes are less pressure sensitive than cracks and permeability is expected to decrease less with depth than for cracks. In the shear zone that we have studied, our observations show a clear difference in the porosity network geometry from pore-tube related connected porosity in the high strained samples, to crack related connected porosity in the undeformed surrounding granite (Fig. 11). The differences in deduced permeabilities (Table 1) are thus expected to be enhanced at confining pressures of about 400 MPa. Consequently, on account of this contrasted structure, channelling of fluid transfer along the shear zone must have been more efficient at depth where ductile deformation occurred.

CONCLUSIONS

In a metre-wide shear zone within a Late Variscan granite intrusion, porosity variations are related to strain. This shear zone presents classical features of heterogeneity and anisotropy: a gradient in the shear strain, which increases from $\gamma = 1$ at the margins to 10 in the median part; the association of *c*-planes and *s*-planes, the angle of which decreases with increasing strain; a grain size reduction toward the median part; and a mineralogical differentiation, with a deformed part richer in micas than the margins.

The current porosity of this ductile shear zone is heterogeneous on a m–cm scale, as demonstrated by NMR imaging, X-ray tomodensitometry, mercury injection porosimetry, and SEM. It ranges between 1% at the margins and 8% in the median part, with throat diameters between 0.8 and 0.01 μm.

The porosity network is mixed and comprises cracks and tubes, as imaged by SEM. Cracks are common in the less deformed samples, whereas tubes prevail in the more strained median part. This shape duality is expected to influence the transfer properties of the studied rocks. The porosity network is anisotropic, especially in the high strained samples, where tubes are preferentially oriented in the *c*-planes. The microscopic anisotropy is shown by SEM observations, together with a possible anisotropic connectivity of cracks and tubes, to produce the macroscopic anisotropy of transfer properties, which accounts for the direction-dependent NMR images at saturation. Permeability values are calculated with a simple model. They are higher in the shear zone (5×10^{-16}–5×10^{-15} m^2) than in the surrounding granite (less than 10^{-17} m^2), which would account for the channelling of fluid transfer along such a zone. Because of the pressure sensitivity of permeability, which is higher for cracks than for tubes, this channelling effect is expected to have been more pronounced at depth, where ductile deformation occurred.

Acknowledgements—We gratefully acknowledge A. Briguet, who gave us access to the NMR Laboratory at Université Claude Bernard in Lyon; and P. Suquet and F. Mazerolle, who permitted us to use the scanner at the Laboratoire de Mécanique et d'Acoustique in Marseille. Special thanks go to Anne Marie Boullier, Jean Pierre Gratier and Elizabeth Charlaix for fruitful discussions, and to Janne Blichert-Toft for kind correction of the manuscript. Reviews by two anonymous referees have been greatly appreciated. This work was supported by CNRS-INSU-IST grant 93TOM15 Tomographie and by CNRS-INSU-DBT Fluides dans la croute, Publication No. 14.

REFERENCES

Bernabé, Y. 1986. The effective pressure law for permeability in Chelmfort granite and Barre granite. *Int. J. Rock Mech. Mining Sci. & geomech. Abstr.* **23**(3), 267–275.

Berthé, D., Choukroune, P. & Jegouzo, P. 1979. Orthogneiss, mylonite and non-coaxial deformation of granites: the example of the South American shear zone. *J. Struct. Geol.* **1**, 31–42.

Brace, W. F. 1980. Permeability of crystalline and argillaceous rocks. *Int. J. Rock Mech. & Mining Sci.*. **17**, 241–251.

Brace, W. F. & Kohlstedt, D. L. 1980. Limits of lithospheric stress imposed by laboratory experiments. *J. geophys. Res.* **85**, 6248–6252.

Brace, W. F., Walsh, J. B. & Frangos, W. T. 1968. Permeability of granite under high pressure. *J. geophys. Res.* **73**(6), 2225–2236.

Dipple, G. M. & Ferry, J. M. 1992. Metasomatism and fluid flow in ductile fault zones. *Contr. Miner. Petrol.* **112**, 149–164.

Dipple, G. M., Wintsch, R. P. & Andrews, M. S. 1990. Identification of the scales of differential element mobility in a ductile fault zone. *J. metam. Geol.* **8**, 645–661.

Etheridge, M. A., Wall, V. J. & Vernon, R. H. 1983. The role of the fluid phase during regional metamorphism and deformation. *J. metam. Geol.* **1**, 205–226.

FitzGerald, J. D. & Stunitz H., 1993. Deformation of granitoids at low metamorphic grade. I: reactions and grain size reduction. *Tectonophysics* **221**, 269–297.

Fyfe, W. S., Price, J. J. & Thompson, A. B. 1978. *Fluids in the Earth's Crust*. Elsevier, Amsterdam.

Gavrilenko, P. & Gueguen, Y. 1989. Pressure dependence of permeability: a model for cracked rocks. *Geophys. J. Int.* **98**, 152–172.

Géraud, Y., Mazerolle, F. & Raynaud, S. 1992. Comparison between connected and overall porosity of thermally stressed granites. *J. Struct. Geol.* **14**, 981–990.

Géraud, Y., Mazerolle, F. & Raynaud, S. 1993. Essai de quantification de la porosité d'un granite altéré: utilisation du scanner médical (tomodensitomètre X). *Bull. Soc. géol. Fr.* **164**, 243–253.

Gueguen, Y. & Palciauskas, V. 1992. *Introduction à la Physique des Roches*. Hermann, Paris.

Guillot, G. & Dupas, A. 1992. NMR imaging applied to water distribution in porous media. In: *Application of NMR Spectrology to Cement Science*. Proceedings International Workshop.

Guillot, G., Kassab, G., Hulin, J. P. & Rigord, P. 1991. Monitoring of tracer dispersion in porous media by NMR imaging. *J. Phys. D: Appl. Phys.* **24**, 763–773.

Gummerson, R. J., Hall, C., Hoff, W. D., Hawkes, R., Holland, G. N. & Moore, W. S. 1979. Unsaturated water flow within porous materials observed by NMR imaging. *Nature* **281**, 56–57.

Guyon, E., Hulin, J. P. & Lenormand, R. 1984. Application de la percolation à la physique des milieux poreux. *Ann. Mines* mai–juin, 17–39.

Jeandey, C., Casagrande, J. M., Briguet, A., Ntoutoume, T. & Guillot, G. 1991. Comparative imaging of liquids in rocks by NMR and differential X-ray CT. *Mat. Res. Soc. Symp. Proc.* **217**, 175–180.

Johns, R. A., Steude, J. S., Castagnier, L. M. & Roberts, P. V. 1993. Nondestructive measurements of fracture aperture in crystalline rock cores using X-ray computed tomography. *J. geophys. Res.* **98**, 1889–1900.

Katz, A. J. & Thompson, A. H. 1987. Prediction of rock electrical conductivity from mercury injection measurements. *J. geophys. Res.* **92**(B1), 599–607.

Kerrich, R., Allison, I., Barnett, R. L., Mos, S. & Starkey, J. 1980. Microstructural and chemical transformations accompanying deformation of a granite in a shear zone at Mieville, Switzerland; with implications for stress corrosion cracking and superplastic flow. *Contr. Miner. Petrol.* **73**, 221–242.

Lespinasse, M. 1984. Contexte structural des gisements d'uranium de la Marche occidentale; fracturation, circulations fluides, propagation de l'episyenitisation. *Mem. CREGU*, Nancy, **8**, 1–196.

Long, J. C. & Witherspoon, P. A. 1985. The relationship of the degree of interconnection to permeability in fracture networks. *J. geophys. Res.* **90**, 3087–3098.

Marquer, D. & Burkhard M. 1992. Fluid circulation, progressive deformation and mass-transfer processes in the upper crust: the example of basement-cover relationships in the External Crystalline Massifs, Switzerland. *J. Struct. Geol.* **14**, 1047–1057.

Marquer, D., Gapais, D. & Capdevila R. 1985. Comportement chimique et orthogneissification d'une granodiorite en faciès schistes verts (Massif de l'Aar, Alpes centrales suisses). *Bull. Mineral.* **108**, 209–221.

Matthews, G. P., Moss, A. K., Spearing, M. C. & Voland, F. 1993. Network calculation of mercury intrusion and absolute permeability in sandstone and other porous media. *Powder Technol.* **76**, 95–107.

Morrow, C. A. & Byerlee, J. D. 1992. Permeability of core samples from Cajou pass scientific drillhole: results from 2100 to 3500 m depth. *J. geophys. Res.* **97**(B4), 5145–5151.

Morrow, C. A. & Lockner, B. A. 1994. Permeability differences between surfaces-derived and deep drillhole core samples. *Geophys. Res. Lett.* **21**(19), 2151–2154.

Potdevin, J. L. & Marquer, D. 1987. Méthodes de quantification des transferts de matière par les fluides dans les roches métamorphiques deformées. *Geodyn. Acta* **1**, 193–206.

Quenardel, J. M., Schmitt, P., Lerouge, G., Cohen-Julien, M., Bouvier, P., Lerebourg, P. & Rolin, P. 1988. Carte géologique de France (1/50 000), feuille Dun-le-Palestel (616), B.R.G.M., Orléans.

Ramsay, J. G. & Graham, R. H. 1970. Strain variation in shear belts. *Can. J. Earth Sci.* **7**, 786–813.

Raynaud, S., Fabre, D., Mazerolle, F., Géraud, Y. & Latière, H. J. 1989. Analysis of the internal structure of rocks and characterisation of mechanical deformation by non-destructive method X-ray tomodensitometry. *Tectonophysics* **159**, 149–159.

Rey, P., Fountain, D. M. & Clement, W. 1994. P-wave velocity across a non coaxial ductile shear zone: consequences for the upper crustal reflectivity. *J. geophys. Res.* **99**, 4533–4548.

Rice, J. R. 1992. Fault stress states, pore pressure distributions, and the weakness of the San Andreas Fault. In: *Fault Mechanics and Transport Properties of Rocks* (edited by Evans, B. & Wong, T. F.). Academic Press, pp. 475–503.

Van Brakel, J., Modry, S. & Svata, M. 1981. Mercury porosimetry: state of the art. *Powder Technol.* **29**, 1–12.

Walsh, J. B. 1965. The effect of crack on the compressibility of rocks. *J. geophys. Res.* **70**(2), 381–389.